ROBOTICS
AND
MECHATRONICS

BILATERAL CONTROL SCHEME FOR SURGICAL
ROBOTIC SYSTEM COLLABORATION

G.Y. (Gregory) Ward

BSC ASSIGNMENT

Committee:
prof. dr. ir. S. Stramigioli
dr. ir. K. Niu
dr. I.S.M. Khalil

July, 2024

UNIVERSITY | TECHMED   UNIVERSITY | DIGITAL SOCIETY
OF TWENTE. | CENTRE   OF TWENTE. | INSTITUTE

Bilateral Control Scheme for Surgical Robotic System Collaboration

Gregory Y. Ward

Abstract—**Robotics holds an ever-growing place within surgery. This paper presents methods introducing a new way of coordinating multiple medical devices during an aortic catheter insertion. This, ultimately, allows for complete automation of the process. We establish the motivation behind the proposed system; hazards faced through fluoroscopy (the imaging technique required in the procedure) are discussed. Furthermore, reasoning as to why collaboration of these systems is beneficial is presented. High-level, kinematic modelling of each system's robotic manipulators allows for catheter control (through joint angle input provided by the operator) and automatic positioning of a C-Arm fluoroscope within the catheter's bending plane. A mathematical model of the fluoroscope's projection creates an artificial image of the catheter and aorta's interior. This completes the system model. Image processing allows for an angle estimation method. Thus, completing the required inputs for the bilateral control scheme. The complete bilateral control method allows for fully automated positioning of the C-Arm fluoroscope. To validate the presented methods, a simulated test bench environment was created. This motivates the feasibility of such a system. Considerations when developing a realistic application, control optimisations and limitations of the proposed system are also included in the concluding section of this paper. The appendices contain in-depth derivations of models and methods used to develop this bilateral control scheme. The concept this paper proves can be applied to many use cases. It opens a new door in medical and collaborative robotics.**

Index Terms—**bilateral control, automated catheter insertion, surgical robotics, collaborative robotics.**

Monday 1st July, 2024

INTRODUCTION

AUTOMATION within medical procedures is ever-increasing. The advantages brought by automation not only lower the risk of certain procedures but also protect surgeons from factors that can have bad implications for their health. Equipment used during surgery can be quite complex and requires specialised operators. It can also be quite tedious to calibrate and position optimally, costing crucial time. During an operation, surgeons and operators must collaborate synchronously to ensure a smooth and successful surgery. This presents the issue that this paper proposes to explore: the automation of surgical equipment for a procedure that requires the collaboration of two robotic systems.

Fluoroscopic Imaging

Fluoroscopy is commonly used within surgery as an imaging technique. This consists of a camera that captures real-time

Dr. Kenan Niu was the acting supervisor of Gregory during this project.

moving images of the inside of a patient using X-rays and a fluorescent screen [1]. This camera is given freedom of movement about the patient by attachment to a frame known as a C-arm. This technique does not come without cost. Being exposed to X-rays can lead to skin injuries and radiation-induced cancer in severe cases. Exposure of ionising radiation to the patient is best kept at a minimum and contained to only regions of interest. Radiation is not only a danger to the patient, but the surgeon will also receive exposure to some levels of radiation. Over time this accumulated exposure could pose a major issue to their health. Another issue faced with medical apparatus is its complexity. When regarding the C-arm, manual operation is no straightforward task; the kinematics of the C-arm body are rather complex and finding the old (optimum) position of the camera after moving it (it obstructs the surgeon for example), can prove to be very time-consuming [2]. Longer time duration leads to higher doses of radiation; this is problematic.

Robotics within Surgery

Evidently the exposure a patient receives can not be avoided, but it could be reduced to the absolute minimum. Full automation of the C-Arm would increase its precision of operation and remove the need for an extra operator to be present in the operating theatre; the C-Arm can be operated through a remote control panel. This saves precious time during surgery, reducing the patient's exposure to the emitted X-rays. Many surgical procedures today, take place with the assistance of robotic systems. In this research, we consider aortic catheter insertion. The catheter is inserted through a small incision made in your groin, chest or top part of your shoulder. This allows for a non-invasive method of placing an aortic valve within a patient [8]. A teleoperated catheter would allow surgeons to be absent from operating theatres during surgery, eliminating any risks they can incur from radiation exposure. Although advantageous, both systems still need to be operated by different persons. One cannot control both simultaneously: it is simply too great of a risk to the patient.

There then lies the gap into which this project explores: creating a control scheme that allows for the C-Arm to follow the catheter, at an optimal position, during its operation. In this way, only the patient would be exposed to radiation, and to a lesser degree. We can take this concept further and devise a fully automated system in which the catheter is inserted completely of its own accord given a projected path within the aorta. This research aims to present methods and prove these through the creation of a simulation environment, to devise a

concept that will open the door to a new way of coordinating multiple medical devices and robots for autonomous catheter navigation.

PROPOSED METHODS

The system can be divided into two main categories: robotic manipulators and image processing methods. Methods for control of each system's dynamics already exist [2], [7] and are not the focus of this research. Instead, high-level control through the kinematics manipulation is proposed. The fluoroscope functions similarly to a light projector. A scaled image of what the X-rays are projected through is perceived. This is modelled to attain an artificial image. In turn, this image is used to realise the complete, bilateral control scheme. Figure 1 shows a block diagram of the complete system.

These methods propose homogeneous transforms. This is imperative for the system proposed as the rotations of different joint frames will be about origins which are not co-located. Homogeneous transformation matrices are in $\mathbb{R}^{4\times4}$ and allow for the combination of translation and rotation transformations into one matrix. To avoid confusion, regardless of whether a manipulator's joint actuates a translation or a rotation, its configuration is still denoted by an angle θ.

C-Arm Manipulation

Forward Kinematics: We model the C-Arm part of the system as a 3 DOF robotic manipulator. A diagram of said manipulator is given in figure 2. Application of screw theory allows for the full transformation, from the base to the end-effector of the manipulator, to be described by equation 1. Background on screw theory relevant to this paper is included in appendix C.

$$g_{\text{st}}(\theta) = e^{\hat{\xi}_1\theta_1}e^{\hat{\xi}_2\theta_2}e^{\hat{\xi}_3\theta_3}g_{\text{st}}(0) \tag{1}$$

The separate matrix exponentials and their derivations are included in appendix D.

We can now evaluate equation 1 as,

$$g_{\text{st}}(\theta) = \begin{bmatrix} R(\theta) & p(\theta) \\ 0_{1\times3} & 1 \end{bmatrix} \tag{2}$$

In which $R \in \mathbb{R}^{3\times3}$ and $p \in \mathbb{R}^3$. To simplify representation let us define $c_i = \cos(\theta_i)$ and $s_i = \sin(\theta_i)$. We can then express $R(\theta)$ as,

$$R(\theta) = \begin{bmatrix} c_1c_3 & -s_1 & c_1s_3 \\ c_3s_1 & c_1 & s_1s_3 \\ -s_3 & 0 & c_3 \end{bmatrix} \tag{3}$$

And $p(\theta)$ as,

$$p(\theta) = \begin{bmatrix} -s_1\left(l_1 + l_2 + \theta_2\right) \\ c_1\left(l_1 + l_2 + \theta_2\right) \\ 0 \end{bmatrix} \tag{4}$$

The full transformation from base to end-effector is now completely described by equation 2.

Inverse Kinematics: The inverse kinematics are derived by way of geometric analysis methods. We begin with the first joint of the C-Arm. This has rotational movement fixated in the x-y plane. An abstraction is shown in figure 3.
Using polar coordinates, the angle of the first joint is straightforward to determine.

Without derivation:

$$\theta_1 = \arctan\frac{p_y}{p_x} \tag{5}$$

The second joint of the C-Arm is now considered. It actuates a translation within the x-y plane. For some angle θ, the difference in magnitude of the end-effector in current and zero configuration gives the joint angle θ_2. An abstraction is given in figure 4.
The joint angle θ_2 is simply the difference in radii.

$$\begin{aligned} \theta_2 &= r_2 - r_1 \\ &= \sqrt{p_{x_0}^2 + p_{y_0}^2} - \sqrt{p_x^2 + p_y^2} \end{aligned} \tag{6}$$

Roboticising a Flexible Catheter

Forward Kinematics: The forward kinematics of the flexible catheter are derived differently from that of the C-Arms'. Two joints shall have their homogenous transformations determined via screw theory, whilst the final joint shall be determined using geometric analysis.

A diagram, defining the relevant parameters of the manipulator, is given in figure 5.

The complete transformation is now described by equation 7.

$$g_{\text{st}}(\theta) = e^{\hat{\xi}_1\theta_1}e^{\hat{\xi}_2\theta_2}T_2^3 g_{\text{st}}(0) \tag{7}$$

The separate matrix exponentials and their derivations are included in appendix E.

Equation 7 is evaluated as,

$$g_{\text{st}}(\theta) = \begin{bmatrix} R(\theta) & p(\theta) \\ 0_{1\times3} & 1 \end{bmatrix} \tag{8}$$

We use the same representations as for the previous transformation Matrix. $R(\theta)$ can then be expressed as,

$$R(\theta) = \begin{bmatrix} c_1c_3 & -c_1c_3 & s_1 \\ s_3 & c_3 & 0 \\ -c_3s_1 & s_1s_3 & c_1 \end{bmatrix} \tag{9}$$

And $p(\theta)$ as,

$$p(\theta) = \begin{bmatrix} c_1\left(l_1 + \frac{l_2}{\theta_3}s_3\right) \\ \theta_2 + \left(\frac{l_2}{\theta_3}\left(1 - c_3\right)\right) \\ -s_1\left(l_1 + \frac{l_2}{\theta_3}s_3\right) \end{bmatrix} \tag{10}$$

Equation 8 now fully describes the transformation from base to end-effector.
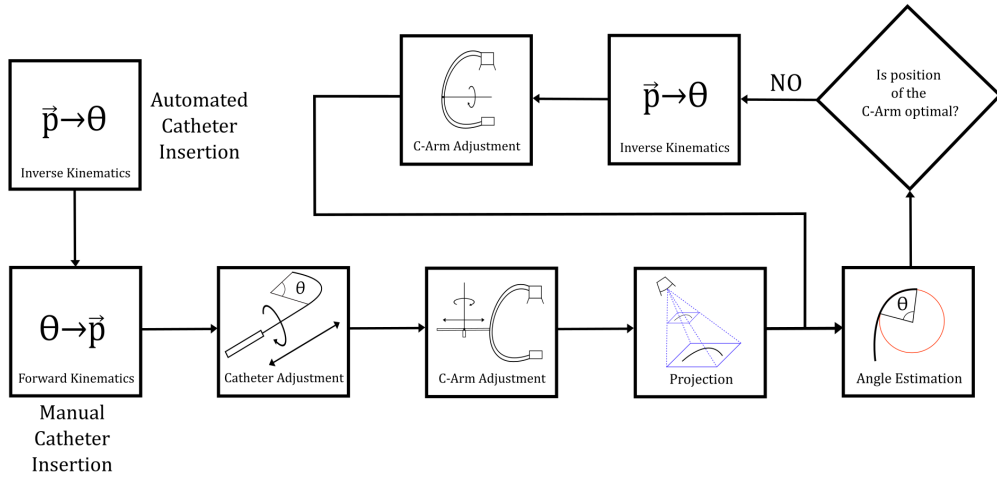
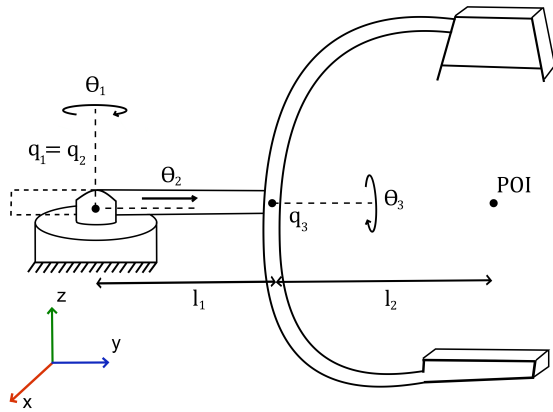Fig. 1: Block diagram presenting an overview of the proposed system.

Fig. 2: A diagram of the proposed C-Arm manipulator defining all relevant parameters. POI (position of interest) is the location of the end-effector.
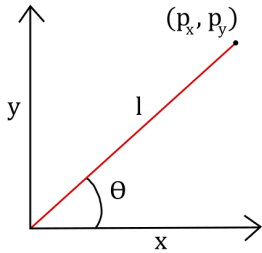

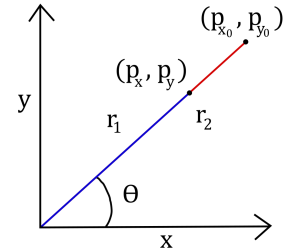Fig. 3: Abstraction of the motion of joint 1.

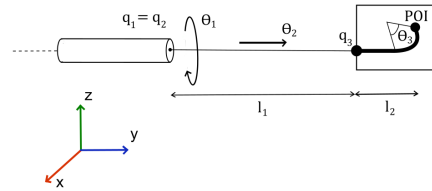Fig. 4: Abstraction of the motion of joint 2.

Fig. 5: A diagram of the proposed flexible catheter manipulator defining all relevant parameters. POI (position of interest) is the location of the end-effector.

Inverse Kinematics: Before deriving the inverse kinematic relationships for the catheter, the DOFs shall be considered. The first joint is revolute about the y-axis. This will affect the rotation of the bending plane of the catheter. The second joint is prismatic along the y-axis. The third, bending joint, has movement within the bending plane.

The prismatic joint is straightforward. An abstraction is shown in figure 4 with $\theta = \frac{\pi}{2}$.

Without derivation,

$$\theta_2 = p_{y_0} - p_y \tag{11}$$

Turning to joint 3, the geometric analysis yields functions that cannot be solved algebraically. Instead, the transcendental function given by equation 47 can be solved to determine the required joint angle. Let,

$$f(\theta_3) = \frac{l}{\theta_3} \sin \theta_3 \tag{12}$$

To determine the solution to this equation we require, θ_3 such that,

$$f(\theta_3) - p_y = 0 \tag{13}$$

The value or values (as there can be infinitely many solutions) that satisfy the above equation will also be the global minimiser or minimisers of the optimisation problem,

$$\min \| f(\theta_3) - p_y \|_2^2 \tag{14}$$

Application of the BFGS (this is detailed in appendix H) algorithm then allows for obtaining an estimation of the required bending angle. Formulating this approach as a minimisation problem, as opposed to the classical root finding problem, reduces the computational complexity. The BFGS algorithm has a computational complexity $\mathcal{O}(n^2)$ as opposed to the $\mathcal{O}(n^3)$ computational complexity of the Newton-Raphson method. The accuracy of employing a minimisation problem to determine the solution will be explored in a later section.

For both manipulators, inverse kinematics to determine θ_3 have not yet been discussed. For the catheter, this is assumed known. The orientation of the aorta can be determined before surgery and will act as a set point for the catheter. The C-Arm requires extra modelling to devise a method that allows for the determining of the required θ_3 for some position. This shall follow.

Fluoroscope Projection and Image Processing

Modelling the Projection: We begin by defining each point on the catheter within the projection window as the set $C = \{p_i \mid p_i \in \mathbb{R}^3\}$. Where, $i \in \mathbb{N}$ is the index of each point within the set. We can now define projection transformation $T_{\text{proj}} : \mathbb{R}^3 \to \mathbb{R}^2$. The projection we wish to model is shown in figure 6.
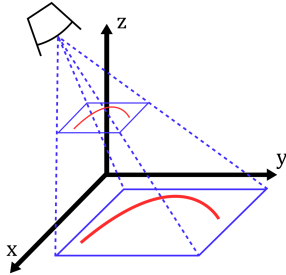

Fig. 6: Diagram depicting the projection of the catheter from $\mathbb{R}^3$ to $\mathbb{R}^2$.

The transform T_{proj} can be expressed as the matrix multiplication of the separate stages of the transformation.

$$T_{\text{proj}} = T_{\text{decomp}} T_{\text{scale}} T_{\text{trans}} T_{\text{persp}} T_{\text{rot}}$$

$$= \begin{bmatrix} \alpha & 0 & \beta & 0 \\ -\frac{\sin\theta(t+b)}{t-b} & -\frac{2n}{r-l} & \frac{\cos\theta(t+b)}{t-b} & 0 \\ 0 & 0 & 0 & 0 \\ \sin\theta & 0 & -\cos\theta & 0 \end{bmatrix} \tag{15}$$

In which,

$$\alpha = \frac{2n\cos\theta - \sin\theta(r+l)}{r-l} \tag{16}$$

And,

$$\beta = \frac{2n\sin\theta + \cos\theta(r+l)}{r-l} \tag{17}$$

The derivations for the entire and separate matrices are included in appendix F.

In applying the transformation T_{proj} to C, we acquire the set $C_P = \{p_i \mid p_i \in \mathbb{R}^2\}$. Where, $i \in \mathbb{N}$ is the index of each point within the set. C_P comprises of all the points on the catheter in the projection space of the C-Arm.

Image Processing: We desire a system that will automate the rotation of the projection plane, upon detecting the rotation of the bending plane. This presents us with an important question: how can we detect the rotation of the bending plane?

(a) 0 rad rotation.   (b) $\frac{\pi}{4}$ rad rotation.   (c) $\frac{\pi}{2}$ rad rotation.
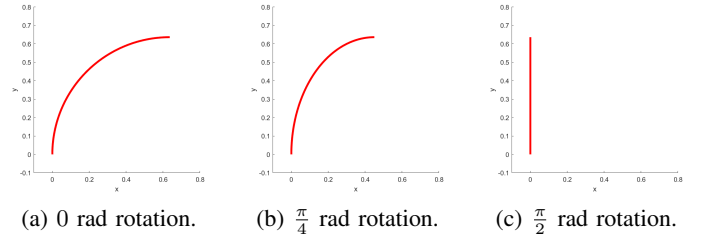
Fig. 7: Catheter tip of length 1 and bending angle $\frac{\pi}{2}$ rad for different angles of rotation.

From a fixed perspective, one perceives a different bending angle depending on the rotation of the catheter's bending plane as shown in figure 7.

An estimate of the bending angle is required to detect this change. The projection model gives us an image of the form shown in figure 8. Its colours have been inverted to make it more realistic.
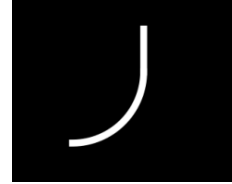

Fig. 8: Artificial image created by the projection model and inversion of colours for a bending angle of $\frac{\pi}{2}$ rad.

It should be noted that, for this research, the artificial image is ideal. Effects of noise, blurring and additional objects within the image are ignored.

Each vector describing a point on the catheter in the pixel space of the image belongs to C_P (as defined in the previous section).

To discern whether a pixel belongs to the background or the catheter, a process known as segmentation must be applied. Regions are formed in the image, with pixels belonging to objects or a specific part of an object within that image. This simplifies analysis [4].

If we let R represent the entire spatial region occupied by the image,

$$R = R_1 \cup R_2 \mid R_1 \cap R_2 = \emptyset \tag{18}$$

In which, R_1 represents the pixels belonging to the catheter and R_2 those belonging to the background.

As the ideal image is simple, thresholding is adequate to segment the image. A histogram of the image's pixel intensities is created. Thresholds are then chosen to section the image into the desired regions of interest. For the artificial image in figure 8 with only 2 regions of interest, thresholding can be used to create a binary image.

Let I_T represent the pixel intensity threshold and $f(x, y)$ the pixel intensity within the image. We can then define $g(x, y)$ as the binary value of that pixel after the threshold has been applied.

$$g(x,y) = \begin{cases} 1 & f(x,y) \geq I_T \\ 0 & f(x,y) < I_T \end{cases} \quad (19)$$

We can reduce the binary objects to a 1-pixel-wide representation to simplify feature extraction. This is called skeletonisation. It entails making successive passes of the image to identify pixel borders which are removed on the condition that the connectivity of the corresponding object is not broken [5]. The image in figure 9 results from all this combined processing.
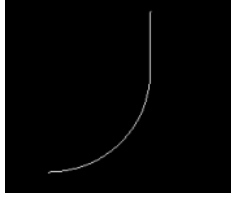

Fig. 9: Artificial image after being segmented and skeletonised.

Extracting the location of each pixel with the binary value corresponding to region R_1 yields the positional vectors belonging to C_P. Figure 10 shows the resulting data from the processed, artificial image.
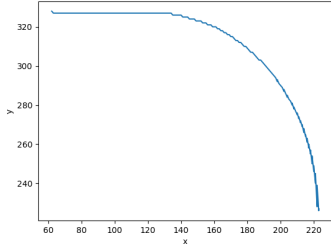

Fig. 10: Graph of points extracted from the artificial image after processing.

Geometrical analysis allows for an angle estimation method; the bending part of the catheter is well-modelled as the segment of a circle. One can obtain the bending angle using the equations of an arc length, namely $l = r\theta$. As l is a known quantity, obtaining the radius r of this circle allows for calculating the bending angle θ.

Acquiring the circle, correlating to the segment acting as the flexible portion of the catheter, can be done using a fitting algorithm. This comprises of solving a minimisation problem to obtain the best estimate of a circle that fits all the points in C_P. An estimate of the angle follows from this. The method of minimisation applied is the method of least squares. Appendix G includes further detail regarding this method. For the vectors belonging to C_P, we define the equation of an ideal circle.

$$\left(x_i - x_c\right)^2 + \left(y_i - y_c\right)^2 = r^2 \quad (20)$$

Where $i \in \mathbb{N}$ is the index of a vector belonging to C_P. We can re-write the expression in the form,

$$ax_i + by_i + c = x_i^2 + y_i^2 \quad (21)$$

In which,

$$\begin{aligned} a &= 2x_c \\ b &= 2y_c \\ c &= r^2 - x_c^2 - y_c^2 \end{aligned} \quad (22)$$

For every vector belonging to C_P, the whole system can be written in matrix form. Let n be the number of vectors belonging to the set C_P. Then,

$$\begin{bmatrix} x_1 & y_1 & 1 \\ x_2 & y_2 & 1 \\ \cdots & \cdots & \cdots \\ x_n & y_n & 1 \end{bmatrix} \cdot \begin{bmatrix} a \\ b \\ c \end{bmatrix} = \begin{bmatrix} x_1^2 + y_1^2 \\ x_2^2 + y_2^2 \\ \cdots \\ x_n^2 + y_n^2 \end{bmatrix} \quad (23)$$

$$Ax = b$$

Where $A \in \mathbb{R}^{n \times 3}$, $x \in \mathbb{R}^3$ and $b \in \mathbb{R}^n$. The optimal solution (as proven in appendix G) to this inconsistent system of equations is given by,

$$\begin{aligned} \hat{x} &= \left(A^T A\right)^{-1} A^T b \\ &= \begin{bmatrix} a \\ b \\ c \end{bmatrix} \end{aligned} \quad (24)$$

Where, $\hat{x} \in \mathbb{R}^3$.

Rearranging the original expression for a, b and c,

$$\begin{aligned} x_c &= \frac{a}{2} \\ y_c &= \frac{b}{2} \\ r &= \frac{\sqrt{4c + a^2 + b^2}}{2} \end{aligned} \quad (25)$$

We obtain the parameters of the best-fitting circle for the vectors in C_P.

Applying the fitting algorithm to the points displayed in figure 10 results in the image shown in figure 11. The effectiveness of this algorithm shall be assessed in a later section of this paper.
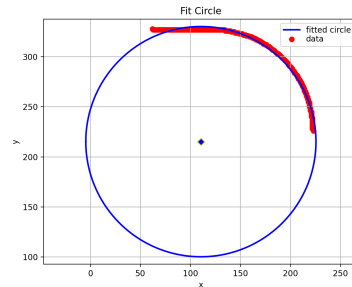

Fig. 11: Resulting circle from applying the fitting algorithm to the points extracted from the artificial image.

CONTROL

For this research, control of the system dynamics is assumed to exist. Control in this context refers to the high-level control of the manipulator kinematics via some algorithm.

Control of the camera position, relative to the position of the catheter tip within its bending plane, requires only the

inverse kinematics of the C-Arm. Catheter tip position can be fed back directly as an input to the kinematics models. Methods of acquiring this position are also assumed to exist. The configuration of the C-Arm manipulator will then adjust depending on the insertion or bending of the catheter within the plane of bending. Figure 12 contains a block diagram of this proposed control structure.
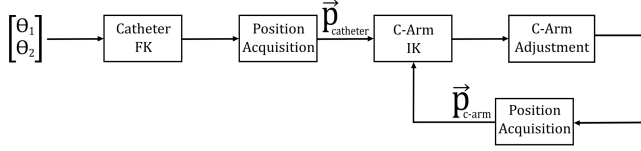

Fig. 12: Block diagram for the control of the C-Arm position within the bending plane. θ_1 and θ_2 are the angles of joints 1 and 2 of the catheter respectively.

Rotation of the catheter relative to the perspective angle of the fluoroscope introduces ambiguity in our angle estimation. The "actual" angle (or best estimate) is the maximum perceived angle by the estimator — rotation of the catheter gives the illusion of the catheter's bending radius increasing, thus, causing a decrease in the estimated bending angle.

The rotation of joint 3 of the catheter is continuous, closed and bounded on the interval $[0, 2\pi]$. We can apply, therefore, the extreme value theorem [6]. Let f be a function representing the estimate of the angle for some rotation of the catheter. It follows that f is continuous, closed and bounded on the interval $[0, 2\pi]$. Hence,

$$f(c) \geq f(x) \geq f(d) \quad \forall x \in [0, 2\pi] \tag{26}$$

In which c, $d \in \mathbb{R}$.

This allows us to create a searching method allowing the C-Arm to determine its optimal position. Initially, the angle estimator defines the current perceived angle. Joint 3 of the C-Arm then rotates left and right of the current angle of joint 3 (by some defined step) and compares the angle perceived at these locations, to the current angle. Upon finding that the perceived angle in one direction increases, the C-Arm continually rotates and re-estimates the angle until the estimate decreases. The largest angle perceived before the estimation began decreasing, is the maximum perceived angle. The C-Arm then defines its optimal position on this basis. Figure 13 gives a block diagram of this control method.
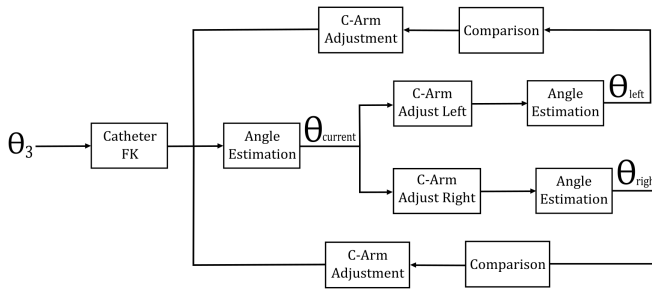

Fig. 13: Block diagram for the control of the C-Arms optimal perspective tracking. θ_3 is the angle of joint 3 of the catheter.

Full system automation is obtained through adding an extra,

preliminary step to the diagram in figure 12. Inverse kinematics of the catheter allow for the following of a planned path. The optimal perspective will again be found via the control strategy depicted in figure 13.

EXPERIMENTAL VALIDATION OF PROPOSED METHODS

Simulator

We prove the feasibility of the proposed system by creating a simulation test bench. This aims to showcase the validity of the models, control and ultimately the effectiveness of the design.

Figure 14 is an image of the simulation environment. Both systems are modelled and an aorta is also visible. The catheter is controlled through joint angle inputs. The window in the bottom right corner displays the projection from the perspective of the fluoroscope receiver.
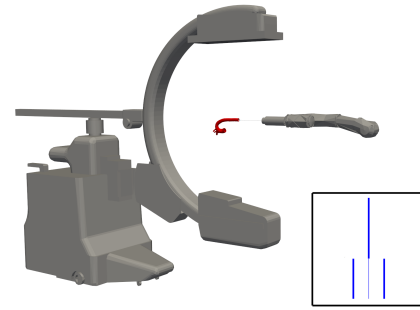

Fig. 14: Overview of the system within the simulation environment.

The catheter model was first simulated in Matlab. Figure 15 depicts the bending joint for various angle inputs. The endpoint is also identified.
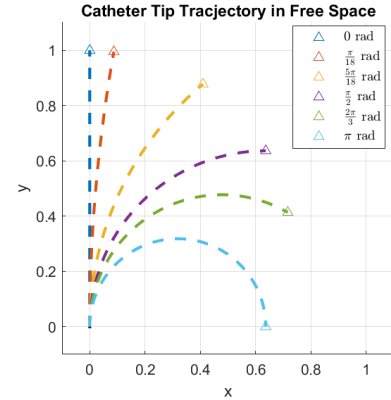

Fig. 15: Plot of the catheter's bending joint for various angles and a length of 1. A triangle marks the endpoint.

The validity of this model within the simulation environment is shown in figure 16.

The projection model produces the correct image. Changing the position of the C-Arm receiver relative to the aorta changes the angle at which it is perceived. Figure 17 shows this for two positions.

Figure 18 displays the result of the searching algorithm and the automated catheter insertion. The camera seeks the optimal position (orthogonal to the bending plane of the aorta) and the catheter calculates the correct joint angles to reach the target.
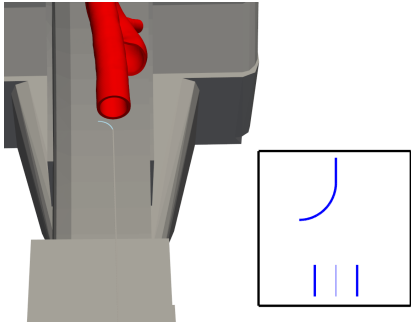
Fig. 16: An image of the simulator depicting the bending joint and its projection for a bending angle of $\frac{\pi}{2}$ rad.
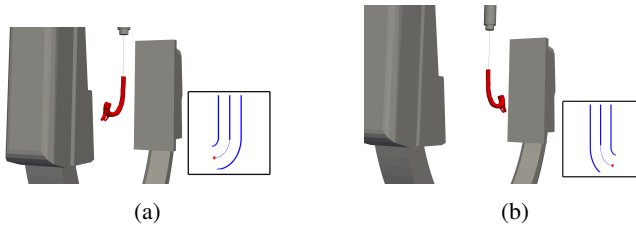

| (a) | (b) |

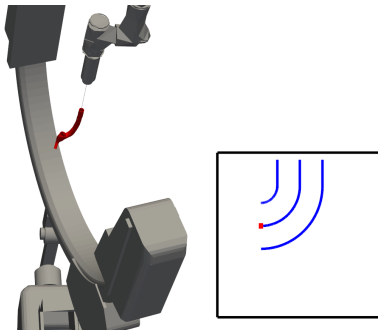Fig. 17: Comparison of aorta projection for different perspectives.

Fig. 18: Example of automated catheter insertion; the target is marked in red.

Evaluation of Manipulator Kinematics

Further validation of the accuracy of the auto-insertion methods is done by comparing the actual and calculated bending angles. The table below lists the actual and calculated angles. The percentage error is also included.

TABLE I: Validation of the bending joint's inverse kinematics

Actual Angle (deg)	Calculated Angle (deg)	Percentage Error (%)
10	0.06	99.4
20	19.97	0.15
30	29.96	0.13
40	39.94	0.15
50	49.93	0.14
60	59.91	0.15
70	69.90	0.14
80	79.88	0.15
90	89.87	0.14

The percentage error for a bending angle of $10 \deg$ is most noticeable. For bending angles below $13 \deg$, the minimisation algorithm used in the inverse kinematics calculations yields a near-zero solution. Initial speculation would suggest that the starting point of the algorithm is incorrect for small angles. This, however, needs further investigation. For angles above $13 \deg$ the inverse kinematics method performs with acceptable degrees of error. Catheter insertion, therefore, is only possible for targets with bending angles $> 13 \deg$.

Assessment of Catheter Angle Estimation

A similar analysis is done to validate the performance of the angle estimator. The results of which are given in the table below.

TABLE II: Validation of the angle estimator

Actual Angle (deg)	Estimated Angle (deg)	Percentage Error (%)
10	9.36	6.40
20	19.40	3.00
30	29.87	0.43
40	38.98	2.55
50	48.85	2.30
60	60.36	0.60
70	69.98	0.03
80	80.54	0.68
90	89.07	1.03

Percentage error is, again, noticeably higher for small angles. For smaller angles, the straight section of the catheter has more influence over the circle fitted in the angle estimation process. A further image processing step to obtain only the curved section of the catheter would help alleviate this issue. Overall, the percentage error is acceptable and proves this estimator to be functional.

DISCUSSION

Summary and Reflection

This research aimed to prove a method of collaborating multiple medical devices in a catheter insertion procedure. Two robotic manipulators were proposed to allow for the control of two medical devices. Kinematics alone allowed for rudimentary C-Arm tracking of the catheter within its bending plane. A mathematical description of the projection created by the fluoroscope was used to create an artificial image. Image processing allowed for angle estimation. A search algorithm that identified the optimal C-Arm position relative to the catheter was proposed. We defined the optimal position as: *"the position at which the "actual" angle (or best estimate) is perceived angle by the estimator"*. This was the maximum possible estimate it could perceive. Moreover, the procedure was fully automated through a path-tracking algorithm. Validation was done by creating a simulation test bench and through experimentation to determine the accuracy of the angle estimator and inverse kinematics methods. Overall, the proposed concept in this paper was deemed feasible.

Initial reflection upon this work considers its necessity. Drawbacks of such a robotic procedure include its extended operating times and increased costs [9]. Such a system, however, would prevent any radiation exposure for the surgeon during the procedure. Methods presented by De Silva et al. [10] propose virtual fluoroscopy to predetermine positioning and ultimately reduce operation and radiation exposure time. This bilateral controller completely removes the need for

C-Arm operation altogether. Work by Kausch et al. [11] already implements a computer algorithm to automate the positioning of the C-Arm. It is a more generic method but is unsuited to automating C-Arm positioning in a dynamic situation. It requires a "pre-scan" of the patient to determine the position where the full anatomy of the patient can be observed. Considering already existing technologies presented by Mätthaus et al. [2] and Namrata et al. [7], the limitations of the models become apparent. The robotic manipulators considered in this paper are greatly simplified. Added model complexity, however, will not change the basis for the bilateral control scheme. What will be affected by a more realistic application are the path-tracking capabilities. Aortas do not follow the same ideal structure as modelled in the simulator. More advanced image processing techniques, such as those presented by Alam [12], to extract the centre line of a real aorta would yield a more robust system.

Development of a Realistic Application

The reflections in the preceding paragraph allow us to identify the requirements for developing a realistic application of the proposed system.

- increased complexity of the manipulator model
- the addition of noise and blurring to make the artificial image less ideal
- realistic model of an aorta
- additional image processing techniques

The manipulators in question will have larger degrees of freedom; the flexible joint will have effects due to hysteresis that require modelling. Additional image processing to acquire the catheter's position within the world frame, segment catheter into straight and bending sections and obtain the central lumen of the aorta is required. Adding bounds to the movement capabilities of the C-Arm would provide useful information on how the controller functions in enclosed spaces.

Optimisation Potential and Limitations of the Proposed System

Optimisation Potential: No consideration of the efficiency of the control method is made currently. Optimising the control of the system can be done with regards to,

- the step size of the C-Arm
- the number of steps for optimal positioning
- the control effort required to obtain the optimal position
- optimising the maximum deviation of the catheter from the planned path during automatic insertion

Optimising system efficiency would greatly reduce the required control effort. System precision would also benefit. Catheter insertion would have much smaller margins of risk (depending on the error within path planning methods).

System Limitations: For small angles, automated catheter insertion is not possible. The inverse kinematics become vastly inaccurate. A small deviation in the initial phases (below a $13\,\text{deg}$ bending angle) of path tracking is observed. As the catheter is narrow, relative to the diameter of the aorta, this deviation is unlikely to cause a collision. An additional initial guess determination step would ensure convergence of the root-finding algorithm to the correct solution.

The system is also limited to bending angles below $90\,\text{deg}$. Above this limit the system's behaviour is unknown. This makes the current system unsuitable for a real application as aorta insertions typically require bending angles above $90\,\text{deg}$. Exploring the difference in system behaviour for bending angles above $90\,\text{deg}$ would lead to a more realistic system.

The effects of latency in the communication between the various control hardware are not modelled. Considering latency poses some questions. How long does an automatic catheter insertion take compared with a manual one? How quickly can the C-Arm position be in response to a positional change of the catheter? Answering these will give further motivation to the benefit of developing such a system and incorporating the proposed methods in other areas of surgical robotics.

CONCLUSION

This paper proposed a new approach to the collaboration of multiple medical devices: a bilateral control scheme allowing for automated control of a C-Arm fluoroscope using a flexible catheter's positional and bending angle as inputs. Not only does this optimise the procedure of catheter insertion, but it also reduces the risk posed by radiation exposure to the surgeon and patient. This control scheme not only allows for C-Arm positioning under manual operation of the catheter, but with the addition of path tracking (for catheter insertion) it allows for complete automation of the procedure.

Analysis methods to derive the inverse and forward kinematics of both systems are presented with the resulting transformation matrices detailed. Forward kinematics are derived as a series of linear transformations extending from the base to the end-effector of each manipulator. Inverse kinematics are derived using a combination of geometric analysis and optimisation (minimisation specifically) methods. The kinematics methods were unproblematic in a manual catheter operation case. With automatic catheter insertion, for small angles, there was inaccuracy in the calculation of the inverse kinematics. This led to deviations from the planned path at small bending angles.

The fluoroscope projection was modelled to allow for the creation of an artificial image. Image processing methods were used to extract information used in the estimation of the bending angle. Exploiting the fact that the perceived angle (for a fixed fluoroscope perspective) is dependent of the rotation of the catheter, a searching algorithm to determine the optimal fluoroscope position was devised. The resulting angle estimator was accurate resulting in a functioning fluoroscope position optimisation strategy.

To prove the feasibility of this concept a test bench simulator was created. This validates the system models and showcases the capabilities of the bilateral controller. The concept that this paper proposes is proven to be feasible and introduces a new approach to automating catheter insertion procedures.

APPENDIX A
AI STATEMENT

APPENDIX B
ROTATION TRANSFORMATION

For the rigid body motions we model in this paper, rotational transformations are required. For completeness, a derivation of the rotational transformation matrix is included. For the translation aspect of the motion, the transformation is deemed trivial. It is simply the addition or subtraction of some translation factor to the coordinate in the axis that we wish to translate along. This is intuitive to understand and is, therefore, not a part of this paper. Deriving the rotational transformation matrix is best done using the diagram in figure 19.
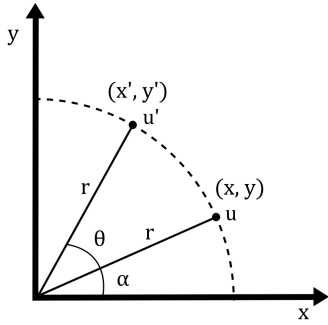

Fig. 19: Diagram showing the rigid body undergoing a rotational transform in $\mathbb{R}^2$.

u is a vector belonging to $\mathbb{R}^2$ and is subject to a rotational transform about the origin. This transformed vector is denoted u'. Using the polar coordinate system, we can define the individual components of the vectors u and u'. For u,

$$x = r \cos \alpha$$
$$y = r \sin \alpha \tag{27}$$

And for u',

$$x' = r \cos (\alpha + \theta)$$
$$y' = r \sin (\alpha + \theta) \tag{28}$$

Now, expanding the expressions for u' give,

$$x' = r \big(\cos \alpha \cos \theta - \sin \alpha \sin \theta \big)$$
$$y' = r \big(\sin \alpha \cos \theta + \cos \alpha \sin \theta \big) \tag{29}$$

And substituting the expression for u,

$$x' = x \cos \theta - y \sin \theta$$
$$y' = x \sin \theta + y \cos \theta \tag{30}$$

We can re-write this in the form of a matrix equation,

$$\begin{bmatrix} x' \\ y' \end{bmatrix} = \begin{bmatrix} \cos \theta & -\sin \theta \\ \sin \theta & \cos \theta \end{bmatrix} \begin{bmatrix} x \\ y \end{bmatrix} \tag{31}$$

We define the rotational transformation matrix $R(\theta)$ as,

$$R(\theta) = \begin{bmatrix} \cos \theta & -\sin \theta \\ \sin \theta & \cos \theta \end{bmatrix} \tag{32}$$

We now wish to determine the $\mathbb{R}^{3 \times 3}$ equivalent of this matrix. A rotation in $\mathbb{R}^3$ only affects the coordinates in the axes about which it does not rotate. In other words, a rotation about some axis will be an identical transformation to that in $\mathbb{R}^2$ within the plane of rotation.

We can now define the rotational matrices about each axis in $\mathbb{R}^3$.
About the x-axis,

$$R_x(\theta) = \begin{bmatrix} 1 & 0 & 0 \\ 0 & \cos \theta & -\sin \theta \\ 0 & \sin \theta & \cos \theta \end{bmatrix} \tag{33}$$

About the y-axis,

$$R_y(\theta) = \begin{bmatrix} \cos \theta & 0 & \sin \theta \\ 0 & 1 & 0 \\ -\sin \theta & 0 & \cos \theta \end{bmatrix} \tag{34}$$

About the z-axis,

$$R_z(\theta) = \begin{bmatrix} \cos \theta & -\sin \theta & 0 \\ \sin \theta & \cos \theta & 0 \\ 0 & 0 & 1 \end{bmatrix} \tag{35}$$

APPENDIX C
SCREW THEORY

Screw theory as presented by Murray [13], is a method for deriving the forward kinematics of serial robotic manipulators. Screw theory works with the basis of screw motions that are used to describe transformations between coordinate frames. Screw motions represent a rotation θ about some axis followed by a translation $h\theta$ parallel to the axis of rotation. Each screw motion has an associated twist ξ. This twist quantifies the associated screw motion. For some rigid body, the exponential of a twist $e^{\hat{\xi}\theta}$ describes its relative motion. It functions as a mapping: taking the initial coordinates to the coordinates after the application of the rigid motion

Chasles [13] stated: *"every rigid body motion can be realised by a rotation about an axis combined with a translation parallel to that axis"*. The exponential of a twist realises this exactly. Application of screw theory allows us to derive a matrix $T \in \mathbb{R}^{4 \times 4}$ which gives a combined description of the translation and rotation of the relevant body frame with respect to the world frame. This has the following form,

$$g_{\text{st}}(\theta) = \begin{bmatrix} R(\theta) & p(\theta) \\ 0_{1 \times 3} & 1 \end{bmatrix} \tag{36}$$

In which $R(\theta)$ is a matrix in $\mathbb{R}^{3 \times 3}$ describing the rotation of the joint about some axis and $p(\theta)$ is a vector in $\mathbb{R}^3$ describing the translation parallel to the axis of rotation.

Now given some set $Q = \{\theta \mid \theta \in [0, 2\pi]\}$, the forward kinematics from base to end-effector of the manipulator is described by the linear transformation $g_{\text{st}} : Q \to SE(3)$. Where $SE(3)$ (the Special Euclidean Group in three dimensions) is a space used to move vectors from one coordinate frame to another [14]. The reader is encouraged to refer to the citation

should they wish to have more information about this space. For interconnected joints, we can form a complete mapping by carrying out consecutive transformations. This is simply (order-dependent) matrix multiplication. We, therefore, define this mapping using the product of exponentials formula.

$$g_{\text{st}}(\theta) = e^{\hat{\xi}_1 \theta_1} \cdots e^{\hat{\xi}_n \theta_n} g_{\text{st}}(0) \tag{37}$$

For revolute joints, the exponential terms in equation 37 can be evaluated using the following expression.

$$e^{\hat{\xi}_i \theta_i} = \begin{bmatrix} e^{\hat{\omega}_i \theta_i} & (I - e^{\hat{\omega}_i \theta_i})(\omega_i \times v_i) \\ 0_{1 \times 3} & 1 \end{bmatrix} \tag{38}$$

Where: $e^{\hat{\xi}_i \theta_i}$ is the rotational matrix in the relevant axis as defined by equations 33, 34 and 35, $\omega_i \in \mathbb{R}^3$ is a unit vector describing the orientation of rotation with respect to the base coordinate frame and $v_i = -\omega_i \times q_i$ in which $q_i \in \mathbb{R}^3$ is the position of the joint respective to the origin.

For prismatic joints, the exponential terms in equation 37 can be evaluated using equation 39.

$$e^{\hat{\xi}_i \theta_i} = \begin{bmatrix} I_{3 \times 3} & v_i \theta_i \\ 0_{1 \times 3} & 1 \end{bmatrix} \tag{39}$$

Where $v_i \in \mathbb{R}^3$ is a unit vector in the direction of translation.

To acquire the full transformation given by 37, one must also obtain $g_{\text{st}}(0)$. This is a matrix describing the transformation from base to end-effector in base configuration.

$$g_{\text{st}}(0) = \begin{bmatrix} I_{3 \times 3} & p(0) \\ 0_{1 \times 3} & 1 \end{bmatrix} \tag{40}$$

APPENDIX D
C-ARM FORWARD KINEMATICS

To begin deriving the forward kinematics of the C-Arm, the relevant parameters of the manipulator must be defined. They are depicted in figure 2. We define $\omega_i \in \mathbb{R}^3$ as the unit vector in the axis of rotation, $v_i \in \mathbb{R}^3$ as the unit vector in the direction of translation and $q_i \in \mathbb{R}^3$ as the positional vector of joint i.

For the two revolute joints:

$$\omega_1 = \begin{bmatrix} 0 \\ 0 \\ 1 \end{bmatrix}$$

$$\omega_3 = \begin{bmatrix} 0 \\ 1 \\ 0 \end{bmatrix}$$

$$q_1 = \begin{bmatrix} 0 \\ 0 \\ 0 \end{bmatrix}$$

$$q_3 = \begin{bmatrix} 0 \\ l_1 \\ 0 \end{bmatrix}$$

And for the prismatic joint:

$$v_2 = \begin{bmatrix} 0 \\ 1 \\ 0 \end{bmatrix}$$

$$q_2 = q_1$$

This yields the following transformation matrices for each joint.

$$e^{\hat{\xi}_1 \theta_1} = \begin{bmatrix} \cos\theta_1 & -\sin\theta_1 & 0 & 0 \\ \sin\theta_1 & \cos\theta_1 & 0 & 0 \\ 0 & 0 & 1 & 0 \\ 0 & 0 & 0 & 1 \end{bmatrix} \tag{41}$$

$$e^{\hat{\xi}_2 \theta_2} = \begin{bmatrix} 1 & 0 & 0 & 0 \\ 0 & 1 & 0 & \theta_2 \\ 0 & 0 & 1 & 0 \\ 0 & 0 & 0 & 1 \end{bmatrix} \tag{42}$$

$$e^{\hat{\xi}_3 \theta_3} = \begin{bmatrix} \cos\theta_3 & 0 & \sin\theta_3 & 0 \\ 0 & 1 & 0 & 0 \\ -\sin\theta_3 & 0 & \cos\theta_3 & 0 \\ 0 & 0 & 0 & 1 \end{bmatrix} \tag{43}$$

Finally, the transformation from base to end-effector in base configuration is given by,

$$g_{\text{st}}(0) = \begin{bmatrix} I_{3 \times 3} & \begin{pmatrix} 0 \\ l_1 + l_2 \\ 0 \end{pmatrix} \\ 0_{1 \times 3} & 1 \end{bmatrix} \tag{44}$$

These, when combined, give the full transformation in equation 1.

APPENDIX E
CATHETER FORWARD KINEMATICS

The revolute and prismatic joints are determined using the following parameters for the catheter manipulator. Again, we define $\omega_i \in \mathbb{R}^3$ as the unit vector in the axis of rotation, $v_i \in \mathbb{R}^3$ as the unit vector in the direction of translation and $q_i \in \mathbb{R}^3$ as the positional vector of joint i.

For the revolute joint:

$$\omega_1 = \begin{bmatrix} 0 \\ 1 \\ 0 \end{bmatrix}$$

$$q_1 = \begin{bmatrix} 0 \\ 0 \\ 0 \end{bmatrix}$$

And for the prismatic joint:

$$v_2 = \begin{bmatrix} 0 \\ 1 \\ 0 \end{bmatrix}$$

$$q_2 = q_1$$

This yields the exponential matrices $e^{\hat{\xi}_1 \theta_1}$ and $e^{\hat{\xi}_2 \theta_2}$ for the two joints.

$$e^{\hat{\xi}_1 \theta_1} = \begin{bmatrix} \cos\theta_1 & 0 & \sin\theta_1 & 0 \\ 0 & 1 & 0 & 0 \\ -\sin\theta_1 & 0 & \cos\theta_1 & 0 \\ 0 & 0 & 0 & 1 \end{bmatrix} \tag{45}$$

$$e^{\hat{\xi}_2 \theta_2} = \begin{bmatrix} 1 & 0 & 0 & 0 \\ 0 & 1 & 0 & \theta_2 \\ 0 & 0 & 1 & 0 \\ 0 & 0 & 0 & 1 \end{bmatrix} \tag{46}$$

The bending joint cannot be determined in the same manner. First, let us consider what a bending transformation would consist of. Relative to the origin, the end-effector will experience a rotation and a translation. The rotation is defined by equation 35: a rotation about the z-axis.

The translation can be determined through geometric analysis. We can consider the catheter as the arc length l of a circle segment with radius r and angle θ. θ is the bending angle, l the (fixed) catheter length and r is the bending radius. l and θ are the known quantities. Figure 20 illustrates an abstraction of this description.
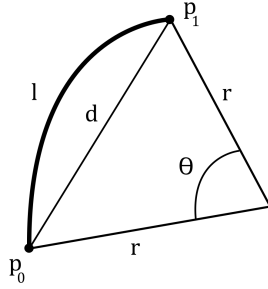

Fig. 20: An abstraction of the catheter tip. The relevant parameters of the bending joint are depicted.

We further simplify the process by creating two sub-problems from our abstraction. These are given by figures 21a and 21b. Referring to figure 21a, an equation for the y component of the catheter tip is easily obtained. We first note the relationship between arc length and radius: $l = r\theta$. Thereafter, application of Pythagoras' theorem gives,

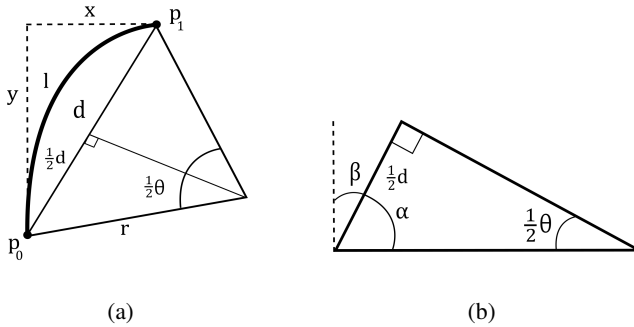$$y = \frac{l}{\theta}\sin(\theta) \tag{47}$$

$$(a) \qquad\qquad (b)$$

Fig. 21: Sub problems devised from the abstraction in figure 20.

The derivation of the x component is more involved. We begin with the sub-problem depicted in figure 21a. Again, by applying Pythagoras' theorem we obtain an expression for d in terms of l and θ.

$$d = 2\frac{l}{\theta}\sin\frac{\theta}{2} \tag{48}$$

Turning to the subproblem in figure 21b, it can be deduced that $\beta = \frac{\theta}{2}$. This, in turn, allows us to acquire an initial expression for x.

$$x = d\sin\frac{\theta}{2} \tag{49}$$

Substituting equation 48 and applying the trigonometric identity $\cos 2\theta = 1 - 2\sin^2\theta$, yields the final expression for x.

$$\begin{aligned} x &= 2\frac{l}{\theta}\sin^2\frac{\theta}{2} \\ &= \frac{l}{\theta}(1 - \cos\theta) \end{aligned} \tag{50}$$

The two transformations (rotation and translation) can now be combined into one bending transformation defined by the matrix T_2^3.

$$T_2^3 = \begin{bmatrix} \cos\theta_3 & -\sin\theta_3 & 0 & \frac{l_2}{\theta_3}(1 - \cos\theta_3) \\ \sin\theta_3 & \cos\theta_3 & 0 & l_1 + \frac{l_2}{\theta_3}\sin\theta_3 \\ 0 & 0 & 1 & 0 \\ 0 & 0 & 0 & 1 \end{bmatrix} \tag{51}$$

For $\theta_3 = 0$ there is a singularity. We account for this by modelling the flexible catheter section as a straight line when it is in its base configuration.

Hence, the corresponding transformation T_2^3 is defined as,

$$T_2^3 = \begin{bmatrix} 1 & 0 & 0 & 0 \\ 0 & 1 & 0 & l_1 + l_2 \\ 0 & 0 & 1 & 0 \\ 0 & 0 & 0 & 1 \end{bmatrix} \tag{52}$$

The two joints determined using screw theory are located at the origin in the base configuration. $g_{\text{st}}(0)$, therefore, is simply $I_{4\times4}$. The distance from the base to the end-effector is modelled in the translation part of the bending transformation.

APPENDIX F
PROJECTION TRANSFORMATION

Before deriving the matrix representation of this projection transformation, we must define the canonical view volume. Within this volume, the view space is normalised such that all points within the camera frustum are contained within a cube. A square pixel aspect ratio is then maintained and the depth of field information is preserved within the 2D image [3].
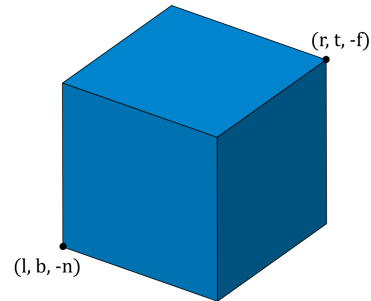

Fig. 22: An abstraction of the Canonical View Volume. This cube is centered at the origin with r = t = n = 1 and l = b = f = −1.

The parameters above are defined as,

  n - near plane
  f - far plane
  l - left plane
  r - right plane

t - top plane
b - bottom plane

The near plane is the plane in which the projected object lies, with the far being the plane in which the projection shall fall. Referring to figure 6, these are defined by a value on the z-axis. The left and right planes are defined by values on the x-axis depending on orientation. It follows that the top and bottom planes are defined by values on the y-axis.

The projection matrix is more easily derived in stages. Initially, one must model the effect of distance between the object and the projection device. This is modelled by a scaling factor proportional to this distance (n in this case). Additionally, to distinguish how near or far an object is within the 2D image, the translation of the object (relative to the centre) must also be included in the transformation.

We define the coordinate system of the object with its z-axis normalised [15] as,

$$(\hat{x}, \hat{y}, \hat{z}) = \left(x\frac{n}{-z}, y\frac{n}{-z}, \frac{az+b}{-z} \right) \tag{53}$$

To obtain normalised coordinates in the z-axis, we enforce the boundary conditions,

$$z = -n \to \hat{z} = -1$$
$$z = -f \to \hat{z} = 1 \tag{54}$$

This allows us to define the system of simultaneous equations,

$$\frac{az+b}{-z} = 1$$
$$\frac{az+b}{-z} = -1 \tag{55}$$
$$\therefore \quad -n = -an + b \quad (1)$$
$$f = -af + b \quad (2)$$

Upon solving, we obtain the following expressions for a and b,

$$a = \frac{-(f+n)}{f-n}$$
$$b = \frac{-2fn}{f-n} \tag{56}$$

This allows us to define the perspective matrix T_{persp} as,

$$T_{\text{persp}} = \begin{bmatrix} n & 0 & 0 & 0 \\ 0 & n & 0 & 0 \\ 0 & 0 & -\frac{f+n}{f-n} & -\frac{2fn}{f-n} \\ 0 & 0 & -1 & 0 \end{bmatrix} \tag{57}$$

To finalise our projection, the result obtained through multiplication with T_{persp} must be translated and scaled. Translation aligns the view volume with the origin and is defined by matrix T_{trans}.

$$T_{\text{trans}} = \begin{bmatrix} 1 & 0 & 0 & -\frac{r+l}{2} \\ 0 & 1 & 0 & -\frac{t+b}{2} \\ 0 & 0 & 1 & -\frac{f+n}{2} \\ 0 & 0 & 0 & 1 \end{bmatrix} \tag{58}$$

Each translation term is simply the midpoint of each plane along the relevant axis.

Scaling transforms the dimensions of the projection to that of the canonical view volumes. The scaling factor is the ratio between the canonical and orthogonal (this is the volume obtained after multiplication with T_{persp}) view volume's dimensions. The scaling transformation T_{scale} is defined as,

$$T_{\text{scale}} = \begin{bmatrix} \frac{2}{r-l} & 0 & 0 & 0 \\ 0 & \frac{2}{t-b} & 0 & 0 \\ 0 & 0 & 1 & 0 \\ 0 & 0 & 0 & 1 \end{bmatrix} \tag{59}$$

For the purpose required in this research, the perception of depth within the image is unnecessary. We therefore only require the x and y coordinates of the vector projections. It is, therefore, necessary to define a transformation matrix T_{decomp} to decompose the vectors from $\mathbb{R}^3 \to \mathbb{R}^2$.

$$T_{\text{decomp}} = \begin{bmatrix} 1 & 0 & 0 & 0 \\ 0 & 1 & 0 & 0 \\ 0 & 0 & 0 & 0 \\ 0 & 0 & 0 & 1 \end{bmatrix} \tag{60}$$

Now the angle of projection is not stationary. As the fluoroscope is rotated about the target object, the perspective angle also changes. This is simply modelled by a transformation matrix T_{rot}. This has rotation defined about the same axis as the C-Arm's third joint. We define T_{rot} for the system parameters defined in figure 2 (origin of rotation is the POI). One should take notice that this is applied foremost as we wish to project from that perspective angle.

$$T_{\text{rot}} = \begin{bmatrix} \cos\theta & 0 & \sin\theta & 0 \\ 0 & 1 & 0 & 0 \\ -\sin\theta & 0 & \cos\theta & 0 \\ 0 & 0 & 0 & 1 \end{bmatrix} \tag{61}$$

APPENDIX G
METHOD OF LEAST-SQUARES

Let us define the matrix $A \in \mathbb{R}^{m \times n}$ and the vector $b \in \mathbb{R}^m$. The method of least-squares provides an approximate solution to an inconsistent matrix equation. Let us define the matrix equation,

$$Ax = b \tag{62}$$

Which is inconsistent and, thus, has no solution.

Now we can define $\hat{x} \in \mathbb{R}^n$ as the optimal solution. This is such that,

$$\|b - A\hat{x}\|_2 \le \|b - Ax\|_2 \tag{63}$$

The optimal solution is acting to minimise the sum of the squares of the difference $b - Ax$.

Now the closest vector of the form Ax to b is the orthogonal projection of b onto $\text{Col}(A)$. Hence, we can define the solution $\hat{x}$ of $Ax = b_{\text{Col}(A)}$ as the least-squares solution.

To derive an expression of the least squares solution we begin by defining $W = \text{Col}(A)$. Now, let $b = b_W + b_{W\perp}$ be the orthogonal decomposition with respect to W. By definition b_W lies in $W = \text{Col}(A)$; there is a vector $\hat{x} \in \mathbb{R}^n$ where $A\hat{x} = b_W$. We know that $b - b_w = b - A\hat{x}$ lies in $W_\perp$ which is equal to $\text{Nul}(A^T)$ [19].

Hence,

$$0 = A^T(b - A\hat{x}) \tag{64}$$

Therefore,

$$A^T A\hat{x} = A^T b \tag{65}$$

For A and b, the following three statements are equivalent,

1. $Ax = b$ has a unique least-squares solution.
2. The columns of A are linearly independent.
3. $A^T A$ is invertible.

$$\therefore \quad \hat{x} = (A^T A)^{-1} A^T b \tag{66}$$

This is the least-squares solution [16].

APPENDIX H
BFGS ALGORITHM

The Broyden-Fletcher-Goldfarb-Shanno (BFGS) algorithm is a method with which one can iteratively solve unconstrained, non-linear optimisation problems [17]. The algorithm's derivation is quite complex and is beyond the scope of this research. The reader is invited to investigate this themselves if they so feel inclined. Here, a description of the algorithm is included to give the reader insight into how it helps solve part of the problem proposed during this research.

Now in an application case of the BFGS algorithm, we wish to minimise $f(x) \mid x \in \mathbb{R}^n$. Note that $f : \mathbb{R}^n \to \mathbb{R}$ is a nonlinear, objective function.

We begin with an initial guess $x_0 \in \mathbb{R}^n$ and initial Hessian $B_0 \in \mathbb{R}^{n \times n}$. From here, the algorithm iterates in the following steps until $x_k \in \mathbb{R}^n$ converges. We first define $p_k \in \mathbb{R}^n$

1. Obtain the direction $p_k \in \mathbb{R}^n$ through solving the equation

$$B_k p_k = -\nabla f(x_k) \tag{67}$$

2. Perform a line search [20] to find an acceptable step size $\alpha_k \in \mathbb{R}$ in the direction found in the initial step. α_k should satisfy the Wolfe conditions [18]. These, in principle, ensure that the gradient converges to 0.
3. Now set $s_k = \alpha_k p_k$, in which $s_k \in \mathbb{R}^n$, and update $x_{k+1} = x_k + s_k$.
4. Let,

$$y_k = \nabla f(x_{k+1}) - \nabla f(x_k) \tag{68}$$

Where $y_k \in \mathbb{R}^n$.

5. Now we can define the next iteration of the Hessian matrix as,

$$B_{k+1} = B_k + \frac{y_k y_k^T}{y_k^T s_k} - \frac{B_k s_k s_k^T B_k^T}{s_k^T B_k s_k} \tag{69}$$

We can determine convergence to the solution by observing the norm of the gradient. For some $\epsilon > 0$, the algorithm may be halted under the condition,

$$\|\nabla f(x_k)\|_2 \leq \epsilon \tag{70}$$

ACKNOWLEDGMENT

REFERENCES

[1] Wikipedia, *Fluroscopy*, https://en.wikipedia.org/wiki/Fluroscopy.
[2] Lars Matthäus, *A Robotic C-arm Fluroscope*, September 2005, Article in International Journal of Medical Robotics and Computer Assisted Surgery.
[3] Notabene, *What is the purpose of the canonical view volume?*, https://gamedev.stackexchange.com/questions/6279.
[4] Wikipedia, *Image Segmentation*, https://en.wikipedia.org/wiki/Image_segmentation.
[5] Scikit-Image, *Skeletonize*, https://scikit-image.org/docs/stable/auto_examples/edges/plot_skeleton.html.
[6] Wikipedia, *Extreme value theorem*, https://en.wikipedia.org/wiki/Extreme_value_theorem.
[7] Nayar Namrata, *Towards the Design and Development of a Robotic Transcatheter Delivery System for MVI*, November 2022, IEEE Trans Med Robot Bionics.
[8] Spire Healthcare, *Transcatheter Aortic Valive Insertion (TAVI)*, https://www.spirehealthcare.com/treatments/heart-treatments/transcatheter-aortic-valve-insertion-tavi/.
[9] Sakashi Bramhe, *Robotic Surgery: A Narrative View*, 15th September 2022, Cureus.
[10] T. De Silva, *C-Arm Positioning Using Virtual Fluoroscopy for Image-Guided Surgery*, 30th May 2017, Proc SPIE Int Soc Opt Eng.
[11] Lisa Kausch, *Toward automatic C-Arm positioning for standard projections in orthopaedic surgery*, 20th May 2020, IJCARS.
[12] Saaed Alam, *An Enhanced Algorithm for Image Processing Based Catheter Selection During Right Coronary Angiography*, 14th December 2020, Cardiology.
[13] Richard M. Murray, *A Mathematical Introduction to Robotic Manipulation*, 1994, Caltech.
[14] Wikipedia, *Euclidean group*, https://en.wikipedia.org/wiki/Euclidean_group.
[15] Emmanuel Agu, *Derivation of Perspective Projection Transformation*, Lecture 6 (Part 3), WPI.
[16] Mathematics LibreText, *The Method of Least Squares*, https://math.libretexts.org/Bookshelves/Linear_Algebra.
[17] Wikipedia, *Broyden-Fletcher-Goldfarb-Shanno Algorithm*, https://en.wikipedia.org/wiki.
[18] Wikipedia, *Wolfe conditions*, https://en.wikipedia.org/wiki.
[19] Mathematics LibreText, *Orthogonal Complements*, https://math.libretexts.org/Bookshelves/Linear_Algebra.
[20] Wikipedia, *Line search*, https://en.wikipedia.org/wiki/Line_search.